# Measurement of the Kerr Nonlinear Refractive Index and its Variation Among 4H-SiC Wafers

Jingwei Li<sup>®</sup>, Ruixuan Wang, Lutong Cai, and Qing Li<sup>®</sup>\*

Department of Electrical and Computer Engineering, Carnegie Mellon University, Pittsburgh, Pennsylvania

15213, USA

(Received 28 November 2022; accepted 2 March 2023; published 24 March 2023)

The unique material property of silicon carbide (SiC) and the recent demonstration of low-loss SiC-on-insulator integrated photonics platform have attracted considerable research interests for chip-scale photonic and quantum applications. Despite the impressive progresses made in SiC photonics, some of its beneficial photonic properties are yet to be fully explored. Here, we carry out a thorough investigation of the Kerr nonlinearity among 4H-SiC wafers from several major wafer manufacturers, and reveal that their Kerr nonlinear refractive index can be significantly different. By eliminating various measurement uncertainties in the four-wave mixing experiment, the best Kerr nonlinear refractive index of 4H-SiC wafers is estimated to be approximately 4 times, instead of the prior estimate of 2 to 3 times, of that of stoichiometric silicon nitride in the telecommunication band. In addition, experimental evidence is developed that the Kerr nonlinearity in 4H-SiC wafers can be stronger along the c axis than that in the orthogonal direction. Our examination of the Kerr nonlinear refractive index also compels a useful correction to the existing model in high-index-contrast waveguides; otherwise, considerable errors can be introduced.

### DOI: 10.1103/PhysRevApplied.19.034083

### I. INTRODUCTION

Silicon carbide (SiC) recently emerged as a promising photonic and quantum material due to its unique properties, including a wide transparency window spanning from the visible to the mid-infrared, simultaneously possessing second- and third-order optical nonlinearities, large thermal conductivity, and the existence of various color centers that can be exploited as single-photon sources or quantum memories [1–3]. In addition, SiC is a robust, CMOS-compatible material with its quality supported by a fast-growing industry, as single-crystal 4H-SiC substrates up to six inches are already commercially available at an affordable cost [4]. These features, coupled with the recent demonstration of a low-loss SiC-on-insulator integrated photonics platform [5–9], portend potential disruption of quantum information processing through scalable integration of SiC-based spin defects with a wealth of quantum electrical and photonic technologies on the same chip [3].

Despite the impressive progresses made in SiC photonics over the past decade, some of its beneficial photonic properties are yet to be fully explored [10]. For example, the Kerr nonlinear refractive index  $n_2$  of SiC, a third-order nonlinear property that underpins optical nonlinear applications such as optical parametric oscillation (OPO) and Kerr frequency comb generation, is

predominantly reported in the literature to be in the range of  $(5-8) \times 10^{-19}$  m<sup>2</sup>/W in the telecommunication band (see Table I). (Note this number is approximately 2–3 times of that of stoichiometric silicon nitride, which is around  $2.5 \times 10^{-19} \text{ m}^2/\text{W}$  at 1550 nm.) However, our recent work suggested that 4H-SiC wafers from different manufacturers seem to yield different levels of Kerr nonlinearity, as  $n_2$  of 4H-SiC from ST Microelectronics (formerly known as Norstel AB and hereinafter referred to as "Norstel" for short) is estimated to be near  $(3.0 \pm$  $1.0) \times 10^{-19}$  m<sup>2</sup>/W for the transverse-electric (TE) modes while that of II-VI Incorporated ("II-VI" for short) 4H-SiC wafers is even lower [11]. A closer look into the literature also exposes the limited data points relied upon by most of the existing works for the  $n_2$  estimation, which tended to ignore various uncertainties in the experiment and thus introduced sizeable errors to the process [11–16].

In this work, a systematic approach for the accurate measurement of the Kerr nonlinearity in 4*H*-SiC wafers is developed. We focus on on-axis, semi-insulating 4*H*-SiC wafers from three major wafer manufacturers, i.e., Norstel, II–VI, and Cree. While both Cree and Norstel SiC wafers are of high purity (i.e., undoped), the II–VI wafers attain high resistivity through vanadium doping, which has been shown to result in color centers that emit single photons in the telecommunication *O* band (1278–1388 nm) [17]. Our study confirms that the Kerr nonlinearities of the aforementioned commercial 4*H*-SiC wafers are indeed significantly different, with Cree wafers

<sup>\*</sup>qingli2@andrew.cmu.edu

TABLE I. Comparison of the measured Kerr nonlinear refractive index of different SiC wafers in the literature versus this work, where various approaches, including cross-phase modulation (XPM), self-phase modulation (SPM), four-wave mixing (FWM), optical parametric oscillation (OPO), and comb generation, are employed. Our work also reveals the larger Kerr nonlinear refractive index for Norstel 4H-SiC wafers along the c axis (//c) compared to the orthogonal direction ( $\perp c$ ). The Cree and II–VI wafers show similar behavior, although their  $n_2$  difference between the two polarizations is smaller and within the measurement uncertainties.

References	SiC polytype	Wafer mfr.	Estimation method	λ (nm)	Kerr $n_2$ $(10^{-19} \text{ m}^2/\text{W})$
Lu et al. [12]	a-3 <i>C</i>		XPM	1550	$5.9 \pm 0.7$
Martini et al. [13]	3C		FWM	1550	$5.31 \pm 0.04$
Cardenas et al. [14]	4H	Norstel	SPM	2360	$8.6 \pm 1.1$
Zheng <i>et al</i> . [15]	4H		FWM	1550	$6.0 \pm 0.6$
Guidry <i>et al.</i> [16,18]	4H	Cree	OPO	1550	$6.9 \pm 1.1$
Cai <i>et al</i> . [11]	4H	Norstel	Comb	1550	$\perp c : 3.0 \pm 1.0$
	4H	II–VI	FWM	1550	$\textbf{2.3} \pm \textbf{0.5}$
This work	4H	Norstel	FWM	1550	$\perp$ <i>c</i> : 3.1 $\pm$ 0.5
					$//c$ : 4.6 $\pm$ 0.6
	4H	Cree	FWM	1550	$\textbf{9.1} \pm \textbf{1.2}$

exhibiting the highest  $n_2$  of  $(9.1 \pm 1.2) \times 10^{-19}$  m<sup>2</sup>/W while II–VI wafers exhibiting the lowest  $n_2$  of  $(2.3 \pm 0.5) \times 10^{-19}$  m<sup>2</sup>/W. For 4*H*-SiC wafers, our work also points to a stronger Kerr nonlinearity along the c axis compared to the orthogonal direction, with the Norstel 4*H*-SiC wafers exhibiting  $n_2$  of  $(4.6 \pm 0.6) \times 10^{-19}$  m<sup>2</sup>/W for the transverse-magnetic (TM, dominant electric field along the c axis) modes and  $n_2$  of  $(3.1 \pm 0.5) \times 10^{-19}$  m<sup>2</sup>/W for the TE modes (dominant electric field orthogonal to the c-axis). Finally, our examination of various waveguide geometries made of the same SiC material also compels a correction to the existing model for the  $n_2$  estimation in high-index-contrast waveguides; otherwise, considerable errors can be introduced.

### II. FWM EXPERIMENT AND y MEASUREMENT

Our approach to determining the Kerr nonlinear refractive index is based on measuring the four-wave mixing (FWM) efficiency between two narrow-linewidth lasers (pump and signal, linewidth <100 kHz) in high-Q SiC microresonators (intrinsic Qs in the range of 1–5 million) [13,15,19]. For this purpose, 4-inch-size SiC-on-insulator (SiCOI) wafers are fabricated using a customized bonding and polishing approach (NGK Insulators) for on-axis, semi-insulating 4H-SiC substrates obtained from Norstel, II–VI, and Cree. After dicing each wafer to  $1 \times 1$  cm<sup>2</sup> chips, we fabricate high-Q SiC microring and racetrack resonators using e-beam lithography and dry etching. In addition, grating couplers are designed to facilitate the input and output coupling between fibers and on-chip waveguides, with typical insertion loss near 5-7 dB at the center wavelength for each grating coupler [11].

As illustrated in Fig. 1, light from the pump laser (Toptica CTL1550, output power fixed at 10 mW) and the signal laser (Agilent 81642A, output power fixed at 1 mW) is combined before being coupled to the on-chip waveguide

through a fiber V-groove array (VGA) [11]. The power of each laser can be externally varied through a variable optical attenuator (VOA) to minimize thermo-optic bistability and higher-order idler generation in the FWM experiment. In addition, the high attenuation accuracy and repeatability (error < 0.1 dB) of VOAs enables an individual estimation of the on-chip power for the pump and signal separately. This is achieved by applying the maximum attenuation (60 dB) to the pump (signal) laser while keeping the normal attenuation level (<15 dB) for the signal (pump) laser, measuring the off-chip powers from the VGA fibers ("in" and "out" ports as illustrated in Fig. 1) using an optical power meter (OPM), and inferring the corresponding on-chip signal (pump) power with the estimated insertion loss. At the output, the pump and signal wavelengths are separated into two paths through a wavelength-division multiplexing (WDM) filter, allowing each of them to be photodetected and tuned to their respective resonances from the transmission scan [20]. Once aligning the pump and signal laser wavelengths to the selected cavity resonances, we measure the idler power, which is generated from the FWM process in the SiC microresonator, using an optical spectrum analyzer (OSA). At this stage, we also tune the pump and signal laser out of resonance and verify that the power measured by OSA is consistent with the number obtained previously from OPM. Such a power calibration scheme proves to be critical as the insertion loss from the chip can deteriorate by 1–2 dB due to unstable fiber-grating alignment during the resonance scan and/or the idler power measurement, resulting in an inaccurate estimation of on-chip powers.

We define the FWM efficiency as the ratio between the idler power (denoted as  $P_i$ , which is the on-chip idler power in the waveguide) and the signal power (denoted as  $P_{s,in}$ , which is the on-chip signal power before entering the SiC microresonator). In the frequency matched scenario, i.e., the pump, signal, and idler are all perfectly aligned

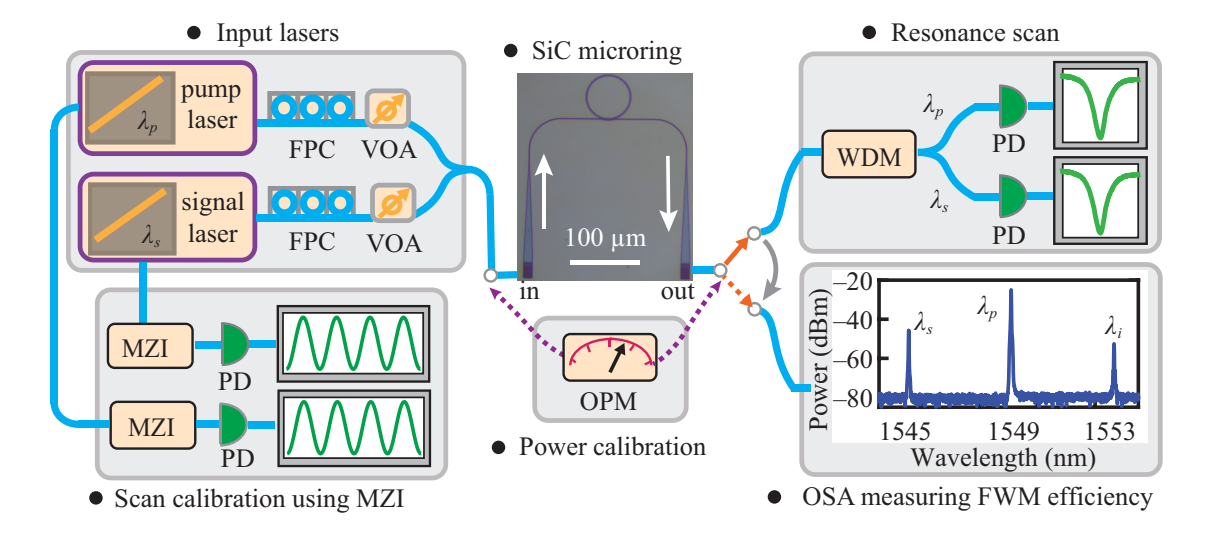


FIG. 1. Experimental schematic for the measurement of the Kerr nonlinearity in SiC microresonators: FPC, fiber polarization controller; VOA, variable optical attenuator; WDM, wavelength-division multiplexer; PD, photodetector; MZI, Mach-Zehnder interferometer; OPM, optical power meter; and OSA, optical spectrum analyzer. Detailed description of the experiment is referred to the main text.

to their respective resonances and their wavelengths are close to each other, this FWM efficiency is given by the following expression [19]:

$$\frac{P_i}{P_{s,\text{in}}} = \left(\frac{2\lambda_p}{\pi n_g \sqrt{L}}\right)^4 \left(\gamma P_{p,\text{in}}\right)^2 \left(\frac{Q_l^2}{Q_c}\right)_p^2 \left(\frac{Q_l^2}{Q_c}\right)_s \left(\frac{Q_l^2}{Q_c}\right)_i,$$
(1)

where  $\lambda_p$  is the pump wavelength;  $n_g$  is the group index of the resonant modes in the C band; L is the circumference of the SiC microresonator;  $\gamma$  is the FWM nonlinear parameter, which is proportional to the Kerr nonlinear refractive index  $n_2$ ;  $P_{p,\text{in}}$  denotes the on-chip pump power before entering the SiC microresonator; and  $Q_L(Q_c)$  is the loaded

(coupling) Q of the resonant mode with the subscripts p, s, i denoting the pump, signal, and idler, respectively. According to Eq. (1),  $\gamma$  is explicitly determined by the following factors:

$$\gamma = \left(\frac{\pi n_g \sqrt{L}}{2\lambda_p}\right)^2 \sqrt{\frac{P_i}{P_{s,\text{in}}}} \frac{1}{P_{p,\text{in}}} \sqrt{\left(\frac{Q_c}{Q_l^2}\right)_p^2 \left(\frac{Q_c}{Q_l^2}\right)_s \left(\frac{Q_c}{Q_l^2}\right)_i},$$
(2)

where the first multiplying factor can be accurately computed given that  $\lambda_p$  and L are known, and  $n_g$  is inferred from the mode's free spectral range [FSR, which is related to  $n_g$  through FSR =  $c/(n_g L)$  with c being the speed of

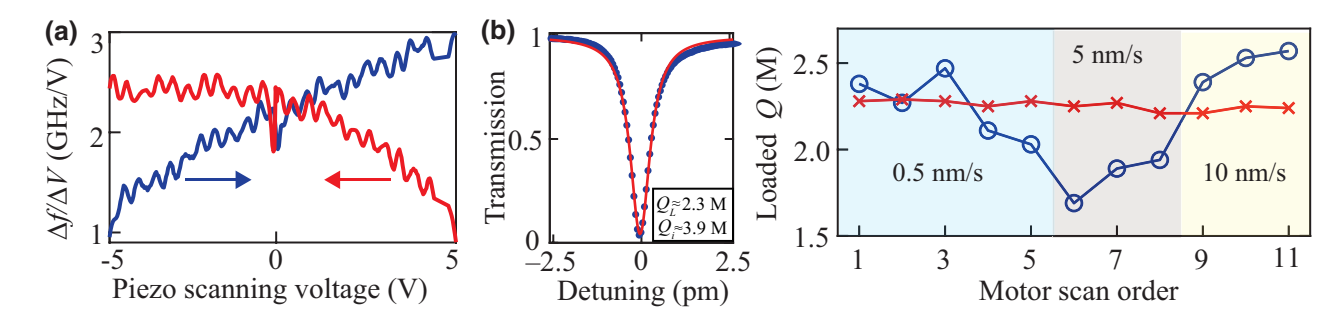


FIG. 2. (a) Nonuniform frequency tuning rate in the piezo scan of the signal laser (Agilent 81642A) characterized by an imbalanced Mach-Zehnder interferometer (MZI, see Fig. 1): the blue and red curves correspond to the forward and backward scan responses at a scan rate of 1 Hz, respectively. (b) Left: swept-wavelength transmission of a representative high-Q resonance in a SiC racetrack microresonator with a bending radius of  $100 \,\mu\text{m}$  [TM<sub>00</sub> in Fig. 3(d)]: the blue dots are the experimental data and the red curve is its Lorentzian fitting, showing a loaded (intrinsic) Q near 2.3 (3.9) million. Right: extracted loaded Qs for the same resonance shown on the left with repeated continuous sweeps from the signal laser. The three colored regions indicate the different tuning speeds varied from 0.5 to 10 nm/s with all the other scanning parameters kept the same: the blue circles are the loaded Qs extracted directly from motor scans (fluctuations up to 20%) and the red crosses are the Qs calibrated using MZI (fluctuations <3%).

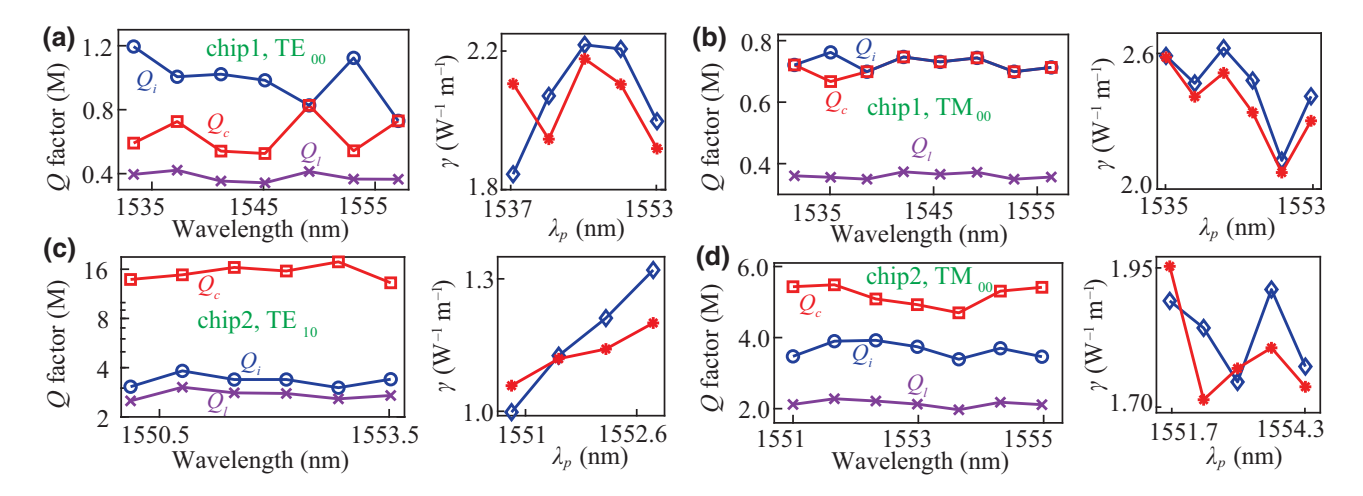


FIG. 3. Experimental results for the  $\gamma$  estimation in four devices from two distinct Norstel SiC chips. For (a)–(d), the left figure shows the measured loaded Q ( $Q_l$ ) as well as inferred intrinsic Q ( $Q_l$ ) and coupling Q ( $Q_c$ ) for various azimuthal orders of the resonances used in the FWM experiment [note the y axis for (c) is in the log scale while the rest is linear]. On the right we plot the extracted  $\gamma$  for the corresponding pump wavelengths, with the signal and idler resonances being 1 FSR away. The blue diamond and red star curves are for the same pump resonance but with the signal and idler positions exchanged. Devices in (a),(b) (from chip 1) are 36- $\mu$ m-radius microrings while devices for (c),(d) (from chip 2) are racetrack resonators with a bending radius of 100  $\mu$ m. Their specific waveguide geometries are provided in Table II.

light in vacuum]. The second multiplying factor in Eq. (2), which is the ratio between the on-chip idler power (after the SiC microresonator) and signal power (before the SiC microresonator), is experimentally determined by tuning the pump laser into resonance and recording the idler power (when the signal is on resonance) and the signal power (when it is off resonance) both from OSA (see Fig. 1). This practice removes uncertainty in the common loss factor shared by the signal and idler, including the insertion loss from the grating coupler and fiber connectors. To address the possibility that this loss factor might be slightly different between the signal and idler, we switch their spectral positions (i.e., set the signal laser at the idler wavelength while keeping the pump the same) and obtain another FWM efficiency for statistical averaging. As such, the FWM efficiency can be reliably measured with an estimated relative uncertainty <10%. The third factor in  $\gamma$  is inversely proportional to the on-chip power for the pump, whose error is predominantly caused by the unstable fiber-grating alignment during the FWM experiment. With our power calibration protocol in place (see discussions following Fig. 1), its relative uncertainty is controlled to be <10%. The final constituent factor in  $\gamma$  indicates the crucial importance of accurate Q estimation, as  $\gamma$  scales as  $Q_c^2/Q_l^4$  and a 10% error in  $Q_l$  can generate up to 20%–40% errors in the  $\gamma$  estimation.

To accurately determine the Q factors from the linear swept-wavelength transmission measurement, we divide a portion of the tunable laser output to a fiber-based MZI, which has a path difference of 3 m and an FSR of 68.1 MHz around 1550 nm (see Fig. 1). By scanning the SiC chip and MZI simultaneously and using the known FSR of the MZI to calibrate the swept wavelengths, we are able to correct various scan nonidealities arising from the limited tuning resolution in tunable lasers. Take the signal laser (Agilent 81642A), for example: the frequency tuning rate of the piezo scan (i.e., varying the laser frequency in a narrow range by applying an external voltage) is found to be nonuniform across a linear voltage scan [Fig. 2(a)]. This directly affects the Q estimation as the inferred cavity linewidth will depend on the relative position of the resonance within the scan

TABLE II. Estimation of the Kerr nonlinear refractive index and the impact of different  $A_{\text{eff}}$  formulas for SiC devices shown in Fig. 3, all of which are made from the same Norstel SiC material.

Norstel devices	Mode	Width (nm)	Height (nm)	Measured $\gamma$ (W <sup>-1</sup> m <sup>-1</sup> )	$n_2$ with Eq. (3) $(10^{-19} \text{ m}^2/\text{W})$	$n_2$ with Eq. (4) $(10^{-19} \text{ m}^2/\text{W})$
Fig. 3(a) Fig. 3(b)	TE <sub>00</sub> TM <sub>00</sub>	$2200 \pm 100$ $2500 \pm 100$	$475 \pm 25$ 475 + 25	$2.05 \pm 0.15$ $2.4 \pm 0.2$	$3.9 \pm 0.6$ $10.0 \pm 2.0$	$3.1 \pm 0.5$ $4.6 \pm 0.6$
Fig. 3(c)	$TE_{10}$	$2500 \pm 100$ $2500 \pm 100$	$850 \pm 50$	$1.15 \pm 0.1$	$4.0 \pm 0.6$	$3.5 \pm 0.6$
Fig. 3(d)	$TM_{00}$	$2500 \pm 100$	$850 \pm 50$	$1.8 \pm 0.1$	$6.3 \pm 0.8$	$5.3 \pm 0.8$

Fig. 3(a)-(b) Air cladding	Mode profile of $ E(x, y) $	$N_{ m eff}$	$N_{\!g}$	$\frac{\left(\iint_{-\infty}^{\infty} \mathrm{E}(x,y) ^2dxdy\right)^2}{\iint_{core} \mathrm{E}(x,y) ^4dxdy}$	$\frac{\left(\iint_{-\infty}^{\infty} \varepsilon_r  E(x,y) ^2 dx dy\right)^2}{\iint_{core} \varepsilon_r^2  E(x,y) ^4 dx dy}$
2200 nm× 475 nm TE <sub>00</sub>	1 μm	2.29	2.73	0.78 μm²	0.69 μm²
2500 nm× 475 nm, TM <sub>00</sub>	1 μm 0	2.15	3.03	1.65 μm²	1.06 μm²

FIG. 4. Computation of two different expressions of  $A_{\text{eff}}$ , i.e., Eqs. (3) and (4), for the waveguide modes corresponding to Figs. 3(a) and 3(b). While numerical values of  $A_{\text{eff}}$  for the TE polarization are reasonably close between the two formulas, their results are more than 2 times different for the TM polarization, which are contributed by the weighted field integral by the relative permittivity and a factor depending on the ratio between  $n_g$  and  $n_0$ . Both waveguides have an oxide cladding underneath and an air cladding on top.

range, which is difficult to control precisely from one scan to another. On the other hand, repeated continuous frequency sweeps from the laser's motor scan also yield 10%–20% fluctuations in the inferred loaded Qs without calibration [Fig. 2(b)]. Such scan nonidealities are ultimately related to the limited wavelength resolution (pm level) present in most of the tunable lasers, which poses a challenge to determining optical Qs accurately on the million level and above. Hence, the introduction of the MZI to this experiment for the scan calibration becomes necessary, which improves the uncertainty in the Ql estimation to be <3% [Fig. 2(b)].

Despite the developed calibration processes for the power and Q measurement, appreciable variations (on the order of 20%–30%) in the  $\gamma$  estimation (and hence  $n_2$ ) still exist. To further reduce the uncertainties, we carry out the FWM experiment on multiple devices for each SiC material so that a statistically meaningful average is obtained. Moreover, different combinations of azimuthal orders in each device are employed to account for the

variations in their intrinsic and coupling Os, which are partially attributed to their scattering-limited radiation losses and frequency-dependent couplings [21]. In Fig. 3, exemplary results for four different devices based on the Norstel SiC (test grade) are presented: the two devices corresponding to Figs. 3(a) and 3(b) are 36-\u03c4m-radius microrings from the SiC chip that has been previously used for the microcomb generation [11], with an approximate SiC thickness around 475 nm; on the other hand, the devices corresponding to Figs. 3(c) and 3(d) are larger racetrack resonators (bending radius of 100 µm and circumference near 1.3 mm), which are fabricated on a different SiC chip with a nominal thickness around 850 nm. To ensure frequency matching between the interacting waves in the FWM process, we choose resonances belonging to the same mode family with only one FSR separation and verify that their dispersion is indeed small enough [11]. The mode order and polarization of each mode family are identified by comparing the measured FSR and coupling Os to the simulation results [21]. While in theory we should

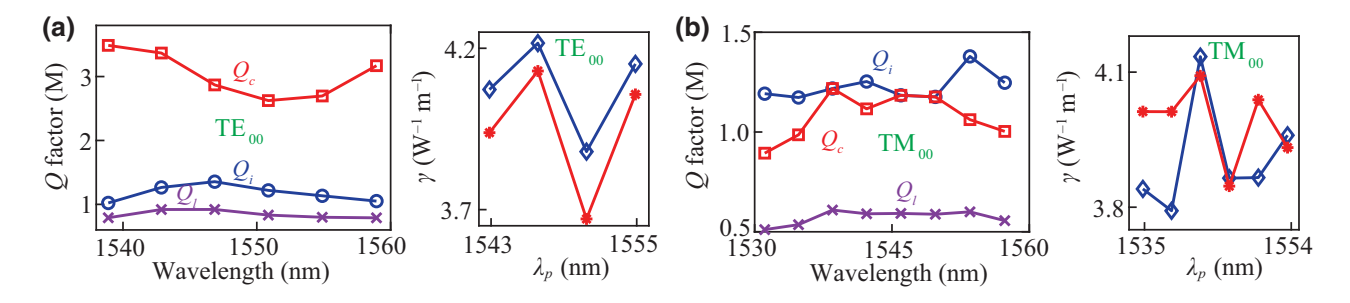


FIG. 5. Experimental results for the  $\gamma$  estimation in two 36- $\mu$ m-radius SiC microrings on a Cree SiC chip. The specific device parameters are listed in Table III. For (a),(b), the left figure shows the measured loaded  $Q(Q_l)$  as well as inferred coupling  $Q(Q_c)$  and intrinsic  $Q(Q_l)$  for the resonances that have been used in the FWM experiment (pump, signal, and idler are only separated by 1 FSR); and on the right we plot the extracted  $\gamma$  for varied pump wavelengths (i.e., different azimuthal orders), with the blue diamond (red star) curve corresponding to the case that the signal wavelength is smaller (larger) than the pump wavelength.

TABLE III. Estimation of the Kerr nonlinear refractive index for the Cree SiC devices shown in Fig. 5. Both devices have an etch depth near 500 nm and a top cladding layer of oxide. The sidewall angle of the device is estimated to be near 80°.

Cree devices	Mode	Width (nm)	Height (nm)	Measured $\gamma$ (W <sup>-1</sup> m <sup>-1</sup> )	$n_2$ with Eq. (3) $(10^{-19} \text{ m}^2/\text{W})$	$n_2$ with Eq. (4) $(10^{-19} \text{ m}^2/\text{W})$
Fig. 5(a)	TE <sub>00</sub>	$2500 \pm 100$	$630 \pm 30$	$4.0 \pm 0.18$	$10.4 \pm 1.2$ $13.6 \pm 1.2$	$8.9 \pm 1.1$
Fig. 5(b)	TM <sub>00</sub>	$2500 \pm 100$	$630 \pm 30$	$3.95 \pm 0.11$		$9.4 \pm 0.9$

expect a uniform  $\gamma$  for the same mode family, the fluctuations observed in Fig. 3 indicate that the aforementioned experimental uncertainties for the  $\gamma$  estimation cannot be completely removed.

## III. n<sub>2</sub> ESTIMATION FROM MEASURED y

After extracting  $\gamma$  from the FWM experiment for each device, the final step in the Kerr nonlinear refractive index measurement is to connect  $\gamma$  to  $n_2$  based on  $\gamma = 2\pi n_2/(\lambda_p A_{\text{eff}})$ , where  $A_{\text{eff}}$  is the effective mode area. The exact definition of  $A_{\text{eff}}$ , however, is not well agreed upon in the literature. For example, one common version of  $A_{\text{eff}}$  that is applicable to low-index-contrast waveguides takes the following form [22]:

$$A_{\text{eff}} = \frac{\left(\iint_{-\infty}^{\infty} |\mathbf{E}(x,y)|^2 dx dy\right)^2}{\iint_{\text{core}} |\mathbf{E}(x,y)|^4 dx dy},\tag{3}$$

where  $\mathbf{E}(x,y)$  is the electric field of the waveguide mode under consideration and x,y are the coordinates in the waveguide cross section. [Note the denominator in Eq. (3) is only integrated within the waveguide core, which is the only material assumed to possess a nonzero  $n_2$ .] For high-index-contrast waveguides, which is the case for SiCOI, we believe that  $A_{\text{eff}}$  needs to be modified as (see derivation in Sec. III.D of the Supplemental Material from Ref. [20]):

$$\tilde{A}_{\text{eff}} = \frac{\left( \iint_{-\infty}^{\infty} \epsilon_r(x, y) |\mathbf{E}(x, y)|^2 dx dy \right)^2}{\iint_{\text{core}} \epsilon_r^2(x, y) |\mathbf{E}(x, y)|^4 dx dy} \left( \frac{n_0}{n_g} \right)^2, \tag{4}$$

where  $\epsilon_r(x,y)$  is the relative permittivity and  $n_0$  denotes the refractive index of the waveguide core ( $n_0$  for the TM and TE polarizations is slightly different given that 4H-SiC is uniaxial). Note that while the first multiplying factor in Eq. (4) resembles the effective mode volume derived in Ref. [23], an additional correcting factor, which depends on the ratio between  $n_0$  and  $n_g$  (group index), is introduced here.

This factor can be intuitively understood based on the fact that  $n_2$  is defined for the bulk material while  $\gamma$  is obtained from confined waveguide modes.

Aside from theoretical justification, experimental evidence for the correct  $A_{\text{eff}}$  can be developed by computing  $n_2$  from the measured  $\gamma$  for various waveguide geometries made of the same material, which should result in a consistent  $n_2$ . Such an example is provided in Table II for the SiC devices measured in Fig. 3. By focusing on the TM polarization, we find that Eq. (3) resulted in dramatically different numerical values of  $n_2$  for the two distinct waveguide geometries corresponding to Figs. 3(b) and 3(d), despite the fact that they are both fabricated from the same Norstel SiC wafer. In contrast, the application of Eq. (4) leads to consistent  $n_2$  (within measurement uncertainties), which lends strong support to its validity. Given the sensitivities of the  $\gamma$  estimation to the Q measurement and the smaller uncertainties in the Q estimation of 36-µmradius microrings compared to those of the larger racetrack resonators, we adopt the  $n_2$  result for the Norstel material in Table I based on Figs. 3(a) and 3(b).

To better understand the difference between the two  $A_{\text{eff}}$ expressions, in particular their reasonable agreement for the TE-polarized modes and significant disagreement for the TM-polarized modes in Table II, we use the waveguide modes corresponding to Figs. 3(a) and 3(b) as an example. As shown in Fig. 4, the TE modes are well confined within the waveguide core and their group index is close to the material index  $n_0$  ( $n_0 \approx 2.6$  at 1550 nm). As a result, the difference between Eqs. (3) and (4) is relatively small. On the other hand, the TM mode expands more outside the waveguide core, given that the vertical dimension is much smaller than the horizontal dimension. This results in a 35% reduction in the field integral of  $A_{\text{eff}}$  by weighting the electric field with the relative permittivity (i.e.,  $\epsilon_r$ ), as done in Eq. (4), compared to the one without [as in Eq. (3)]. In addition, Eq. (4) has another multiplying factor that depends on the ratio between  $n_0$  and  $n_g$ . Because

TABLE IV. Estimation of the Kerr nonlinear refractive index for the II–VI SiC devices shown in Fig. 6. Note both devices have an etch depth near 500 nm and a top cladding of air. The sidewall angle of the device is estimated to be near 80°.

II–VI devices	Mode	Width (nm)	Height (nm)	Measured $\gamma$ (W <sup>-1</sup> m <sup>-1</sup> )	$n_2$ with Eq. (3) $(10^{-19} \text{ m}^2/\text{W})$	$n_2$ with Eq. (4) $(10^{-19} \text{ m}^2/\text{W})$
Fig. 6(a) Fig. 6(b)	${ m TE_{00}} \ { m TM_{00}}$	$2500 \pm 100$ $3000 \pm 100$	$600 \pm 30$ $600 \pm 30$	$0.96 \pm 0.08$ $0.98 \pm 0.07$	$2.3 \pm 0.3$ $3.9 \pm 0.4$	$2.0 \pm 0.3$ $2.5 \pm 0.4$

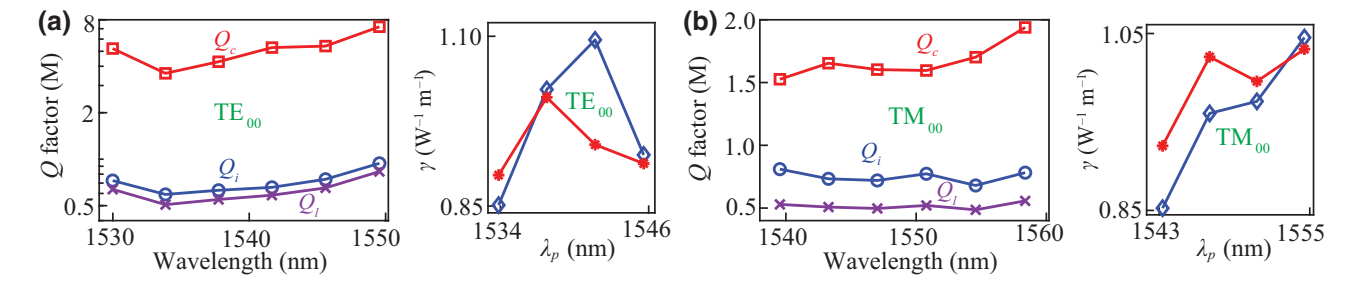


FIG. 6. Experimental results for the  $\gamma$  estimation in two devices from the same II–VI SiC chip. The specific device parameters are listed in Table IV. For (a),(b), the left figure shows the measured loaded  $Q(Q_l)$  as well as inferred coupling  $Q(Q_c)$  and intrinsic  $Q(Q_l)$  for the resonances that have been used in the FWM experiment (pump, signal, and idler are only separated by 1 FSR); and on the right we plot the extracted  $\gamma$  for varied pump wavelengths (i.e., different azimuthal orders), with the blue diamond (red star) curve corresponding to the case that the signal wavelength is smaller (larger) than the pump wavelength. Note that the  $\gamma$  axis in (a) is in the log scale as the coupling Qs of the TE<sub>00</sub> mode family are much larger than the intrinsic Qs (i.e., undercoupled).

the group index  $n_g$  for the TM mode is considerably larger than  $n_0$ , this factor will contribute another 30% reduction in the effective mode area. Combined together, the numerical value of  $A_{\rm eff}$  given by Eq. (4) is approximately 46% of that obtained with Eq. (3) for the waveguide mode corresponding to Fig. 3(b). We believe the data presented in this paper unanimously supports the adoption of Eq. (4) as the general formula for connecting  $\gamma$  to  $n_2$ , while Eq. (3) is only applicable for the waveguide mode that is well confined in the waveguide core and whose group index is similar to the refractive index of the bulk material.

# IV. $\gamma$ MEASUREMENT AND $n_2$ ESTIMATION FOR CREE SiC

We perform similar device fabrication and FWM measurements for the Cree SiC (production grade) wafer as we did for the Norstel material. The Cree chip has an estimated thickness of  $(630 \pm 30)$  nm based on reflectometry. The SiC microrings have a radius of  $36~\mu m$  and varied ring widths. In the dry-etching step, we remove approximately 500-nm SiC (calibrated using profilometer), leaving a pedestal layer with a nominal thickness around 130 nm. In the end of the fabrication, a 1- $\mu m$ -thick PECVD oxide layer is deposited on top of the SiC devices.

In Fig. 5, we present exemplary results for the TE and TM resonances supported by the SiC microrings. Using

the extracted  $\gamma$ , we estimate  $n_2$  in Table III by taking the uncertainties in the waveguide dimensions into consideration. While the mean value of  $n_2$  for the TM polarization (whose dominant electric field is along the c axis) is slightly bigger than that of the TE polarization (whose dominant electric field is orthogonal to the c axis), this difference (approximately equal to 5%) is within the measurement error and is not statistically significant. Therefore, we averaged  $n_2$  for the TE and TM polarizations in Table I and increased its uncertainty slightly to account for both cases.

# V. $\gamma$ MEASUREMENT AND $n_2$ ESTIMATION FOR II–VI SiC

Likewise, we fabricate 36- $\mu$ m-radius SiC microrings on semi-insulating II–VI 4*H*-SiC (primary grade) chips and perform FWM experiments to extract their  $\gamma$  and  $n_2$ . The II–VI chip has an estimated SiC thickness of  $(600 \pm 30)$  nm based on reflectometry. In the dry-etching process, we remove approximately 500-nm SiC, leaving a pedestal layer with a nominal thickness around 100 nm. For this chip, the top cladding is air.

In Fig. 6,we present representative results for the TE and TM resonances supported by the SiC microrings. As can be seen, the mean value of  $n_2$  along the c axis (TM) is approximately 20%–30% larger than that of the orthogonal direction (TE). Nevertheless, this difference is still within

TABLE V. Summary of the experimental results for the  $TE_{00}$  mode family in 36- $\mu$ m-radius SiC microrings made from semi-insulating, on-axis 4*H*-SiC wafers from three major wafer manufacturers. The two  $A_{\text{eff}}$  expressions [i.e., Eqs. (3) and Eq. (4)] provide a reasonably close estimation of  $n_2$  for each material, confirming that its numerical values are indeed significantly different among 4*H*-SiC wafers produced by II–VI, Norstel, and Cree.

SiC mfr.	Fig.	Width (nm)	Height (nm)	Measured $\gamma$ (W <sup>-1</sup> m <sup>-1</sup> )	$n_2$ with Eq. (3) $(10^{-19} \text{ m}^2/\text{W})$	$n_2$ with Eq. (4) $(10^{-19} \text{ m}^2/\text{W})$
II–VI	6(a)	$2500 \pm 100$	$600 \pm 30$	$0.96 \pm 0.08$	$2.3 \pm 0.3$	$2.0 \pm 0.3$
Norstel	3(a)	$2200 \pm 100$	$475 \pm 25$	$2.05 \pm 0.15$	$3.9 \pm 0.6$	$3.1 \pm 0.5$
Cree	5(a)	$2500 \pm 100$	$630 \pm 30$	$4.0 \pm 0.18$	$10.4 \pm 1.2$	$8.9 \pm 1.1$

the measurement uncertainties. As such, we take the averaged  $n_2$  for the TE and TM polarizations in Table I, and increased its uncertainty to account for both cases.

#### VI. DISCUSSIONS

We want to emphasize that one of the main conclusions of this work, that the Kerr nonlinear refractive index  $n_2$  from the three major SiC wafer manufacturers is significantly different, is unlikely to be caused by the errors introduced in the connection from the experimentally measured  $\gamma$  to  $n_2$ . This is because we can focus on the TE-polarized modes that are well confined in the in-plane direction (waveguide widths  $>2~\mu$ m), for which different  $A_{\rm eff}$  expressions yield similar results (see Table V). Such variations are likely a result of different growth methods adopted by these wafer manufacturers. For 4H-SiC wafers from the same manufacturer, our experience based on multiple (>5) II–VI wafers suggests that the measured Kerr nonlinearity is fairly uniform without noticeable differences.

### VII. CONCLUSION

In conclusion, we develop a systematic approach for the accurate measurement of the Kerr nonlinearity in 4H-SiC wafers, and show that there are significant variations in the Kerr nonlinear refractive index among 4H-SiC wafers from different manufacturers. Our work also reveals a larger Kerr nonlinearity along the c axis than that in the orthogonal direction, and a useful correction in the modeling of  $n_2$  to obtain consistent results in high-index-contrast waveguides. We believe these findings, in particular the fact that the Kerr nonlinear refractive index of 4H-SiC can be up to 4 times (instead of the prior estimate of 2 to 3 times) of that of stoichiometric silicon nitride, are crucial to the future development of the SiCOI platform for a variety of nonlinear applications in both the classical and quantum regimes.

## **ACKNOWLEDGMENTS**

This work is supported by DARPA (D19AP00033) and NSF (2127499). The authors would like to thank the helpful discussions with Professor Robert Davis from CMU and equipment support from Dr Lijun Ma and Dr Oliver Slattery at NIST. J. Li also acknowledges the support of Axel Berny Graduate Fellowship from CMU.

[1] C. P. Anderson, A. Bourassa, K. C. Miao, G. Wolfowicz, P. J. Mintun, A. L. Crook, H. Abe, J. U. Hassan, N. T. Son, T. Ohshima, and D. D. Awschalom, Electrical and optical control of single spins integrated in scalable semiconductor devices, Science 366, 1225 (2019).

- [2] S. Castelletto, and A. Boretti, Silicon carbide color centers for quantum applications, J. Phys.: Photonics **2**, 022001 (2020)
- [3] D. M. Lukin, M. A. Guidry, and J. Vučković, Integrated Quantum Photonics with Silicon Carbide: Challenges and Prospects, PRX Quantum 1, 020102 (2020).
- [4] T. Kimoto, Material science and device physics in SiC technology for high-voltage power devices, Jpn. J. Appl. Phys. **54**, 040103 (2015).
- [5] X. Lu, J. Y. Lee, P. X.-L. Feng, and Q. Lin, Silicon carbide microdisk resonator, Opt. Lett. 38, 1304 (2013).
- [6] T. Fan, H. Moradinejad, X. Wu, A. A. Eftekhar, and A. Adibi, High-Q integrated photonic microresonators on 3C-SiC-on-insulator (SiCOI) platform, Opt. Express 26, 25814 (2018).
- [7] B.-S. Song, T. Asano, S. Jeon, H. Kim, C. Chen, D. D. Kang, and S. Noda, Ultrahigh-Q photonic crystal nanocavities based on 4H silicon carbide, Optica 6, 991 (2019).
- [8] D. M. Lukin, C. Dory, M. A. Guidry, K. Y. Yang, S. D. Mishra, R. Trivedi, M. Radulaski, S. Sun, D. Vercruysse, G. H. Ahn, and J. Vučković, 4H-silicon-carbide-on-insulator for integrated quantum and nonlinear photonics, Nat. Photonics 14, 330 (2020).
- [9] C. Wang, Z. Fang, A. Yi, B. Yang, Z. Wang, L. Zhou, C. Shen, Y. Zhu, Y. Zhou, R. Bao, Z. Li, Y. Chen, K. Huang, J. Zhang, Y. Cheng, and X. Ou, High-Q microresonators on 4H-silicon-carbide-on-insulator platform for nonlinear photonics, Light: Sci. Appl. 10, 139 (2021).
- [10] A. Yi, C. Wang, L. Zhou, Y. Zhu, S. Zhang, T. You, J. Zhang, and X. Ou, Silicon carbide for integrated photonics, Appl. Phys. Rev. 9, 031302 (2022).
- [11] L. Cai, J. Li, R. Wang, and Q. Li, Octave-spanning microcomb generation in 4H-silicon-carbide-on-insulator photonics platform, Photonics Res. 10, 870 (2022).
- [12] X. Lu, J. Y. Lee, S. Rogers, and Q. Lin, Optical Kerr nonlinearity in a high-*Q* silicon carbide microresonator, Opt. Express **22**, 30826 (2014).
- [13] F. Martini, and A. Politi, Four wave mixing in 3C SiC ring resonators, Appl. Phys. Lett. 112, 251110 (2018).
- [14] J. Cardenas, M. Yu, Y. Okawachi, C. B. Poitras, R. K. W. Lau, A. Dutt, A. L. Gaeta, and M. Lipson, Optical non-linearities in high-confinement silicon carbide waveguides, Opt. Lett. 40, 4138 (2015).
- [15] Y. Zheng, M. Pu, A. Yi, X. Ou, and H. Ou, 4H-SiC microring resonators for nonlinear integrated photonics, Opt. Lett. 44, 5784 (2019).
- [16] M. A. Guidry, K. Y. Yang, D. M. Lukin, A. Markosyan, J. Yang, M. M. Fejer, and J. Vučković, Optical parametric oscillation in silicon carbide nanophotonics, Optica 7, 1139 (2020).
- [17] G. Wolfowicz, C. P. Anderson, B. Diler, O. G. Poluektov, F. J. Heremans, and D. D. Awschalom, Vanadium spin qubits as telecom quantum emitters in silicon carbide, Sci. Adv. 6, eaaz1192 (2020).
- [18] M. A. Guidry, D. M. Lukin, K. Y. Yang, R. Trivedi, and J. Vučković, Quantum optics of soliton microcombs, Nat. Photonics 16, 52 (2022).
- [19] P. P. Absil, J. V. Hryniewicz, B. E. Little, P. S. Cho, R. A. Wilson, L. G. Joneckis, and P.-T. Ho, Wavelength

- conversion in GaAs micro-ring resonators, Opt. Lett. 25, 554 (2000).
- [20] Q. Li, M. Davanço, and K. Srinivasan, Efficient and low-noise single-photon-level frequency conversion interfaces using silicon nanophotonics, Nat. Photonics 10, 406 (2016).
- [21] Q. Li, A. A. Eftekhar, Z. Xia, and A. Adibi, Azimuthal-order variations of surface-roughness-induced mode
- splitting and scattering loss in high-*Q* microdisk resonators, Opt. Lett. **37**, 1586 (2012).
- [22] G. P. Agrawal, *Nonlinear Fiber Optics* (Academic Press, San Diego, 2019), 6th ed.
- [23] Q. Lin, T. J. Johnson, R. Perahia, C. P. Michael, and O. J. Painter, A proposal for highly tunable optical parametric oscillation in silicon micro-resonators, Opt. Express 16, 10596 (2008).